Acta Materialia 218 (2021) 117232

Contents lists available at ScienceDirect

Acta Materialia

journal homepage: www.elsevier.com/locate/actamat

Full Length Article

Strain glass state in Ni-rich Ni-Ti-Zr shape memory alloys

S. Xu[a], J. Pons[a,*], R. Santamarta[a], I. Karaman[b], O. Benafan[c], R.D. Noebe[c]

[a] Departament de Física, Universitat de les Illes Balears, Palma de Mallorca 07122, Spain
[b] Department of Materials Science and Engineering, Texas A&M University, College Station, TX 77843, USA
[c] Materials and Structures Division, NASA Glenn Research Center, Cleveland, OH 44135, USA

ARTICLE INFO

Article history:
Received 15 January 2021
Revised 16 July 2021
Accepted 3 August 2021
Available online 7 August 2021

Keywords:
Strain glass
Martensitic phase transformation
Ni-Ti-Zr
Shape memory alloys
Elinvar effect

ABSTRACT

This work reports the existence of the strain glass state in Ni-rich Ni-Ti-Zr shape memory alloys induced by the precursor stages of the H-phase precipitation, typical of this alloy system. The strain glass is detected from dynamic mechanical testing and microstructural observations by electron diffraction and Transmission Electron Microscopy (TEM). The elastic modulus measurements also suggest the *elinvar* effect in these alloys. The strain glass state of this material exhibits superelastic effect in compression with recoverable strain levels over 4% and very little temperature dependence of the stress-strain curves over a temperature range of 230 to 300 K.

1. Introduction

The thermoelastic martensitic transformation (MT) is a diffusionless solid state phase transition that results in special properties such as the shape memory effect and superelasticity. The low symmetry martensite phase is formed from the high symmetry parent phase (austenite) upon cooling or mechanical loading. The domains of martensite phase correspond to different orientation variants of the martensitic crystal structure and exhibit twinning relationships to accommodate the strain emerged during the transition. Under an external stress, the martensitic domains reorient towards the variants most favored by the applied stress, producing a macroscopic strain in the material. This behavior is denoted as *ferroelasticity*, in analogy with ferromagnetism or ferroelectricity. In the latter systems, the ferroic property is the magnetization/electric polarization, which can be tuned by an external field through reorientation of magnetic/electric domains. For ferroelastic shape memory alloys, the lattice strain constitutes the ferroic degree of freedom.

A normal martensitic transformation, or ferroelastic transition, is accompanied by the formation of relatively large martensite domains with a uniform lattice strain. This situation can be interpreted as a long-range ordering of lattice strains. However, a novel state of locally disordered lattice strain was found in alloys with suppressed ferroelastic transition, denoted as *strain glass* [1]. The strain glass (SG) state appears in systems containing nanometric sized spatial heterogeneities that frustrate the long-range ordering of lattice strains typical for the ferroelastic transition. For the first reported cases of SG, the spatial heterogeneity was created by point defects, *i.e.* excess Ni atoms in Ni-rich binary Ni-Ti or Ni-Ti-X (X = Fe, Co, Cr, Mn, Pd, Nb) [2–6]. Other sources of spatial heterogeneities leading to the SG state have been identified. These include the onset of Ni_4Ti_3 precipitation in Ni-Ti alloys resulting in nanometric precipitates [7], severe plastic deformation forming dense dislocation tangles [8,9] and atomic order with nanometric sized ordered domains and antiphase boundaries in Ni-Co-Mn-In [10]. Strain glass has been reported in many different SMA systems, including Fe-based alloys [11,12], Ti-based alloys [13–15], ferromagnetic Ni-Mn-Ga-Co and Ni-Fe-Ga-Co [16–19] and metamagnetic SMAs [10,20,21].

The SG state is typically identified from low frequency dynamic mechanical tests. The alloys with normal martensitic transformation present a maximum in the internal friction (*IF*) temperature evolution and a minimum in the elastic modulus (*E*) at the phase transition, and the peak temperature is independent of the frequency of the applied alternating stress. Conversely, the materials with SG state exhibit much lower modulus minima and *IF* maxima and these anomalies show a clear frequency dependence, following a Vogel-Fulcher relationship [1]. This is, in fact, the main signature of the SG state. The origin of such anomalies in the modulus and internal friction signals is attributed to the freezing of "martensitic-like" disordered nanodomains (which are "frustrated" from developing into large martensite plates due to the spatial heterogeneity existing in the system) into a glassy state with no

* Corresponding author.
E-mail address: jaume.pons@uib.es (J. Pons).

https://doi.org/10.1016/j.actamat.2021.117232

long-range correlation [1]. However, in a study using low and high (ultrasonic) frequencies and alloys with different Ni contents, the *IF* and *E* anomalies were interpreted as relaxational premartensitic anelasticity [22]. In the frozen (or relaxed) state, the average crystal structure is the cubic austenite. However, the electron diffraction patterns exhibit prominent streaking developing diffuse spots at positions close to those corresponding to the martensite phase (or R phase in Ni-rich Ni-Ti), concomitant with a mottled contrast in conventional TEM images and randomly distributed nanodomains revealed by HRTEM [1,15,23–25]. This is another distinctive feature of the SG state.

Over the same timeframe that the concept of strain glass was being developed, large research efforts were also focused on development of Ni-rich Ni-Ti-Hf and Ni-Ti-Zr alloys with elevated martensitic transformation temperatures, as cheaper alternatives to the Ni-Ti-Pd or Ni-Ti-Pt high temperature shape memory alloys [26–46]. The Ni-rich Ni-Ti-Hf/Zr alloys can be strengthened by nanoprecipitation of the so-called H-phase, which increases the dimensional stability of the material for shape memory and superelastic effects and its cyclic responses. The H-phase, which is not formed in binary Ni-Ti alloys, is described as a superstructure of the B2 phase obtained from a recombination of the Hf/Zr and Ti atoms in their sublattice, followed by shuffling of all the atoms [47,48]. However, in a recent work by some of the present authors, the B2-phase of the $Ni_{50.3}Ti_{29.7}Zr_{20}$ alloy was shown to be unstable upon prolonged ageing at 520 K and to undergo short range atomic reordering processes in the B2 phase producing diffuse streaks in the diffraction patterns, with a concomitant suppression of the thermal martensitic transformation [49].

The present work reports new results about the instability of the B2 phase in $Ni_{50.3}Ti_{29.7}Zr_{20}$ and $Ni_{50.9}Ti_{24.1}Zr_{25}$ alloys. It will be shown that both alloys exhibit suppressed martensitic transformation as well as other features that are commonly associated with the strain glass state.

2. Experimental methods

Two alloys with nominal compositions of $Ni_{50.3}Ti_{29.7}Zr_{20}$ at.% (alloy 1) and $Ni_{50.9}Ti_{24.1}Zr_{25}$ at.% (alloy 2) were vacuum induction melted from high purity elemental constituents of Ni, Ti and Zr (99.98%, 99.95% and 99.9%, respectively) under argon atmosphere in a graphite crucible, and subsequently cast into a copper mold. The resulting ingots were homogenized at 1320 K for 72 h, sealed in mild steel cans and hot extruded at 1170 K with an area reduction of 7:1. Samples were cut from the extruded rods using electrodischarge machining (EDM) or a low-speed diamond saw. Then, the samples were encapsulated in quartz ampoules under partial Ar atmosphere and solution heat treated (SHT) at 1170 K for 1 h followed by water quenching (WQ) by breaking the ampoule. Subsequently, some SHT specimens were subjected to isothermal aging treatments at 520 K in air followed by WQ.

Differential Scanning Calorimetry (DSC) measurements were performed in a Mettler-Toledo DSC823e unit at cooling/heating rate of 10 K/min. Low frequency cyclic mechanical characterization was performed in a Dynamic Mechanical Analyzer (DMA) Q800 from TA Instruments in the single cantilever mode under a fixed strain amplitude of 0.05% and a frequency range of the oscillating stress between 0.2 and 20 Hz. The elastic storage modulus (*E)* and internal friction (*IF* or tan δ, δ being the phase shift between the oscillating stress and strain) signals were recorded in the temperature range from 370 K to the lowest temperature ($\sim$ 200 K) achievable by the liquid nitrogen cooling system. Uniaxial mechanical tests in compression were conducted on a Zwick Z100 materials testing machine at a strain rate of 5.3×10^{-4} s^{-1} to investigate superelastic behavior at different temperatures. Custom made compression plates were used to change the sample temperature by thermal conduction through the plates, which were equipped with electric heaters driven by PID temperature controllers. Cooling was achieved by cold nitrogen flowing through copper coils wrapped around the grips. X-ray diffractometry (Bruker D8 Advance, equipped with a cooling chamber) was used to investigate the crystal structure of the samples at low temperatures. The microstructural characterization was performed by Transmission Electron Microscopy (Hitachi H600 at 100 kV, FEI Tecnai G2 F20 at 200 kV) with an *in-situ* cooling sample holder. The TEM samples were double jet electropolished in a solution of 30% nitric acid in methanol at 250 K.

3. Experimental results

3.1. Thermal characterization

The main results of the DSC tests are summarized in Fig. 1. The alloy 1 ($Ni_{50.3}Ti_{29.7}Zr_{20}$) after SHT exhibits exothermic and endothermic peaks characteristic of the forward and reverse martensitic transformation, respectively (Fig. 1a). However, the MT characteristics have poor reproducibility and depend on the rapidity of the ampoule breaking and water quenching process. In fact, intentional delays in breaking the ampoules to reduce the quenching rate have been shown to lead to a complete suppression of the MT in $Ni_{50.3}Ti_{29.7}Zr_{20}$ when measured by DSC [49]. Fig. 1a also presents the DSC thermograms of the SHT sample after subsequent ageing treatments in air at 520 K for different times. The transformation peaks are progressively shifted to lower temperatures and diminished in area until their complete suppression in the DSC signal after 12 h ageing at 520 K.

Suppression of the martensitic transformation was also observed in alloy 2, even after SHT. None of the tested SHT samples of $Ni_{50.9}Ti_{24.1}Zr_{25}$, even with high quenching rate, exhibited transformation peaks in the DSC, as shown in Fig. 1b. Therefore, in the alloy with higher Ni and Zr content, the thermal martensitic transformation is already suppressed just after the solution heat treatment, without any additional ageing. It is worth noting that a thermal martensitic transformation was detected in both alloys in the as-extruded state (hot extrusion at 1170 K, prior to the SHT treatment), as shown in Fig. 1b for alloy 2. In this state, alloy 2 contains H-phase precipitates formed during air cooling after the hot extrusion process. The microstructure of the alloys will be further discussed in Section 3.2. For alloy 1, the transformation temperatures for the as-extruded and solution heat treated states are very similar to each other.

Fig. 2 presents the elastic modulus and internal friction curves obtained by DMA for $Ni_{50.3}Ti_{29.7}Zr_{20}$. In the SHT state (Fig. 2a), the *IF* data present clear peaks around 235 K related to the thermal martensitic transformation and the peak temperature is frequency independent. The *IF* peaks observed in Fig. 2a are considerably broadened in relation to the DSC peaks of Fig. 1a. This is a consequence of the large size of the DMA sample and possible existence of temperature gradients along its length. The storage elastic modulus does not show the typical dip observed in most SMAs, for which *E* decreases upon cooling in the austenite state and then increases during the martensitic transformation. Instead, the elastic modulus is practically temperature independent in the austenite state (*elinvar* effect) and then starts to increase upon cooling concomitantly with the martensitic transformation. Fig. 2b and c correspond to the SHT sample aged at 520 K for 12 h (treatment that completes the MT suppression in the DSC, Fig. 1a) and 10 days, respectively. In these cases, the curves only present a slight frequency dependence in the low temperature side. However, after extending the ageing treatment at 520 K to 14 or 16 days, a clear frequency dependence appears in the *E* and *IF* signals at low temperatures (Fig. 2d,e). The storage modulus data show again a

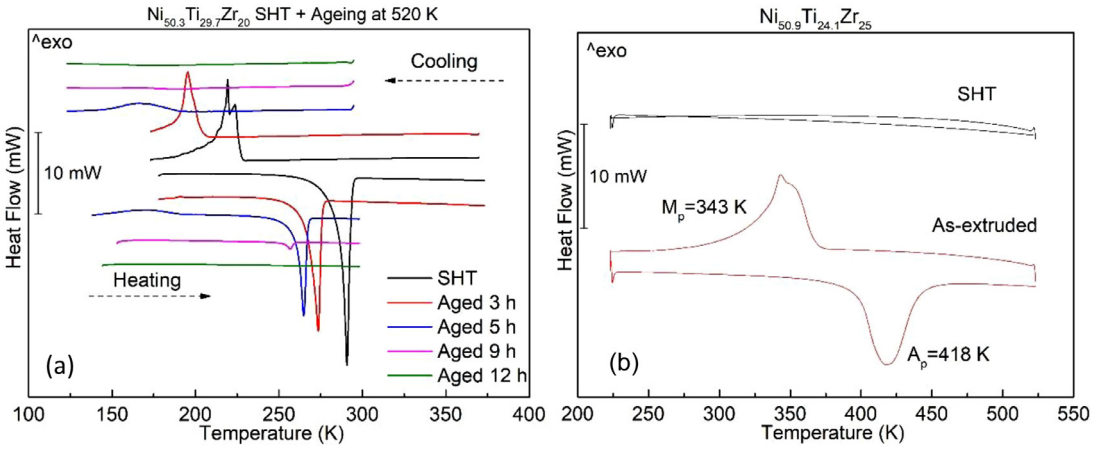

Fig. 1. DSC cooling and heating runs in the solution heat-treated (SHT) state and as a function of the ageing time at 520 K for the $Ni_{50.3}Ti_{29.7}Zr_{20}$ alloy (a) and in the SHT and as-extruded states for a $Ni_{50.9}Ti_{24.1}Zr_{25}$ alloy (b).

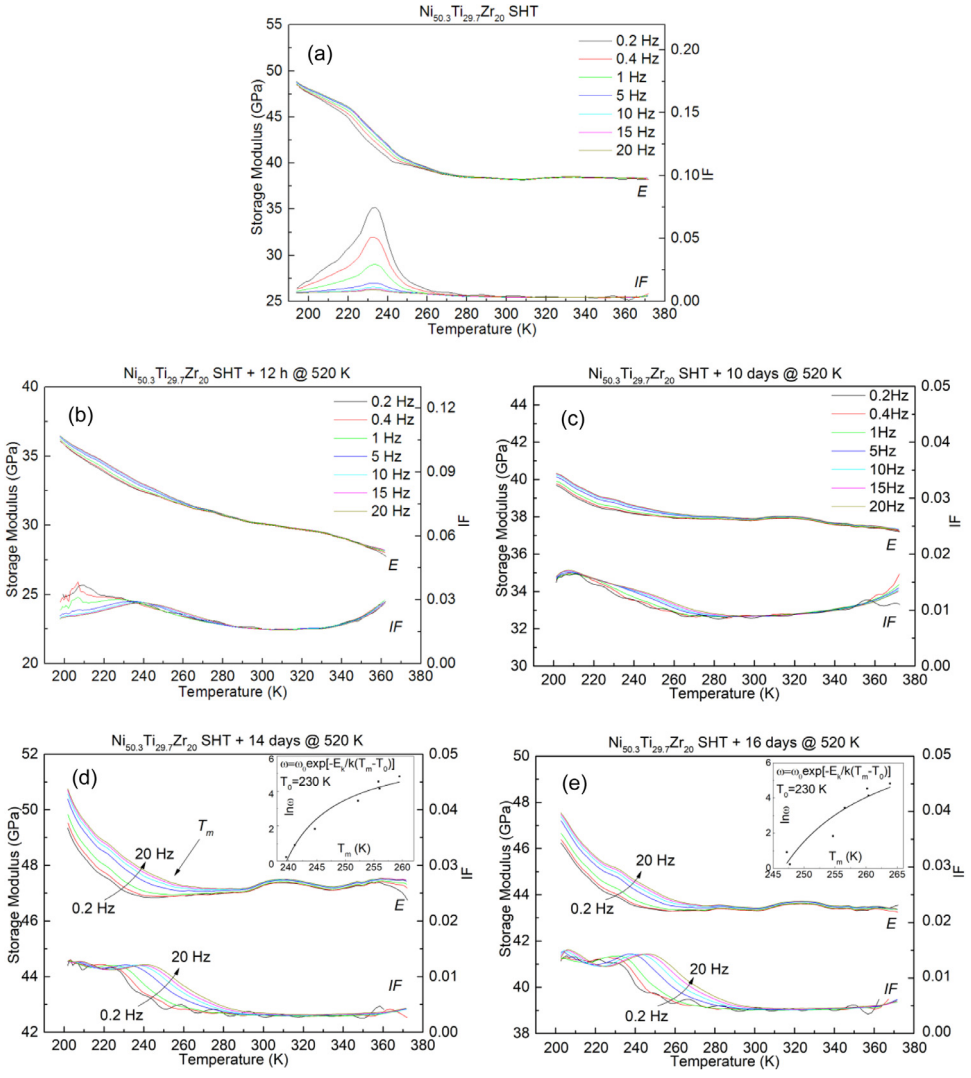

Fig. 2. Storage elastic modulus (E) and internal friction (IF) for the $Ni_{50.3}Ti_{29.7}Zr_{20}$ alloy in (a) the SHT state and after ageing treatments at 520 K for (b) 12 h, (c) 10 days, (d) 14 days and (e) 16 days. Insets in (d,e) show a semilogarithmic plot of the frequencies as a function of T_m together with the Vogel-Fulcher fitting to obtain the strain glass freezing temperature (T_0).

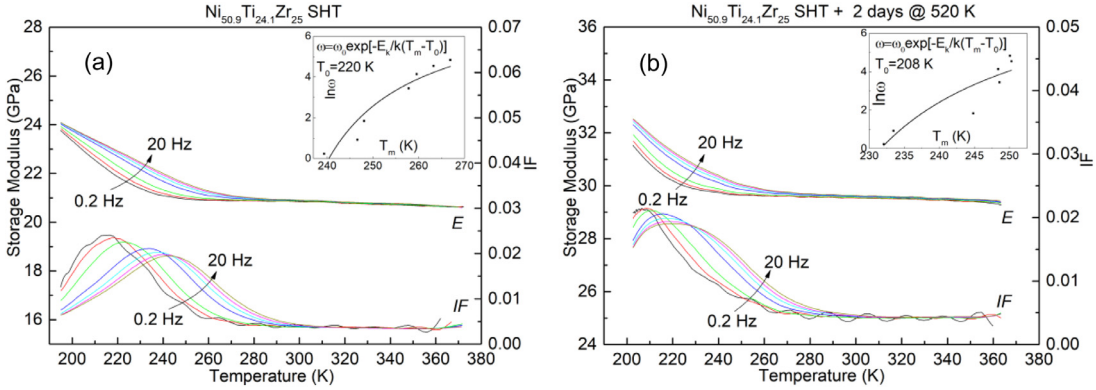

Fig. 3. Storage elastic modulus (E) and internal friction (IF) for $Ni_{50.9}Ti_{24.1}Zr_{25}$ alloy in (a) the SHT state and (b) after ageing at 520 K for 2 h. Insets show a semilogarithmic plot of the frequencies as a function of T_m together with the Vogel-Fulcher fitting to obtain the strain glass freezing temperature (T_0).

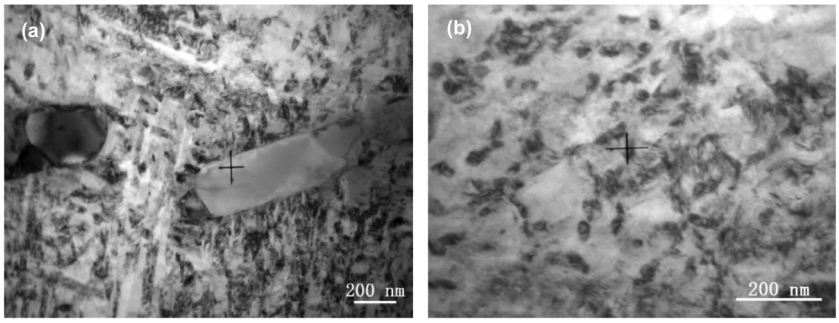

Fig. 4. Micrographs at different magnification of as-extruded $Ni_{50.9}Ti_{24.17}Zr_{25}$ showing (a) martensite plates together with oxide and carbide inclusions and (b) H-phase precipitates embedded in the martensitic matrix.

rather flat curve at higher temperatures followed by an increase after some level of cooling. The temperature of the modulus "minimum", T_m, has been taken at the point where the signal starts to increase from the nearly constant regime, as indicated by an arrow in Fig. 2d for the curve at 20 Hz. The values of T_m obtained at different frequencies ω fit reasonably well with a Vogel-Fulcher-type equation, $\omega = \omega_0 \exp[-E_a/k_B(T_m - T_0)]$, as shown in the inset of Fig. 2d,e. The ideal freezing temperature T_0 obtained from the fitting is $T_0 = 230$ K in both cases.

Fig. 3 a corresponds to the alloy 2 ($Ni_{50.9}Ti_{24.1}Zr_{25}$) in the SHT state, without any additional ageing. Again, clear frequency-dependent anomalies appear in both IF and E curves at low temperatures that fit the Vogel-Fulcher equation with $T_0 = 220$ K. An additional ageing at 520 K for 2 days shifts the T_0 temperature to 208 K (Fig. 3b). Therefore, the DMA results are consistent with a strain glass state developed in the $Ni_{50.3}Ti_{29.7}Zr_{20}$ after SHT and prolonged ageing at 520 K and in the $Ni_{50.9}Ti_{24.1}Zr_{25}$ alloy just after the SHT treatment without any additional ageing.

3.2. Structural and microstructural characterization

The general microstructure of the alloys after casting and hot extrusion contains some large particles (Fig. 4a) identified as oxide and carbide inclusions (mostly ZrC), formed as a consequence of carbon diffusion from the graphite crucibles used for induction melting. Moreover, H-phase precipitates of a few tens of nm in size are also present in alloy 2, as shown in Fig. 4b, whereas alloy 1 is free of H phase in the as-extruded condition. The H-phase precipitates in alloy 2 were formed during the slow air cooling of the hot extruded rod, which was surrounded by a steel layer from the original canning material, due to the enhanced driving force for precipitation arising from the composition of this alloy. With such a microstructure, the martensitic transformation takes place in the as-extruded alloy 2, as commented in the previous section (Fig. 1b). In fact, martensite plates containing the H-phase precipitates are visible in Fig. 4. The solution heat treatment, performed at 1170 K after hot extrusion, dissolves the H-phase precipitates and the subsequent water quenching prevents their renewed formation, in such a way that the SHT samples are only composed of the B2 phase (transformable to B19' martensite in alloy 1) and the occasional oxide and carbide inclusions. These inclusions are considered not to play a significant role on the main focus of the present study.

Fig. 5 presents selected-area electron diffraction patterns (SADP) of the $[001]_{B2}$ zone axis taken in different conditions. For the $Ni_{50.3}Ti_{29.7}Zr_{20}$ alloy in the SHT state, the pattern at room temperature consists of sharp reflections of the B2 phase accompanied by very little diffuse intensity (Fig. 5a). However, the diffuse intensity at room temperature increases significantly after ageing for 14 days at 520 K (Fig. 5b) and also in the $Ni_{50.9}Ti_{24.1}Zr_{25}$ alloy after SHT with no additional ageing (Fig. 5d), corresponding to states with suppressed MT and well established strain glass state. The diffuse streaks are close to the positions of superlattice spots characteristic of the H phase, which have been marked in Fig. 5b by blue and red spots. This will be further discussed in Section 4. In fact, similar diffuse streaks were reported by Lu et al. in $Ni_{52}Ti_{42}Zr_6$ and were attributed to short range ordering of the Zr atoms as a previous step to the formation of precipitates by aging at 770 K [27,28]. The patterns in Fig. 5c,e were taken at 120 K for both alloys. At this temperature (below the frequency-dependent anomalies in E and IF signals), the streaking forms more prominent diffuse spots around the B2 fundamental reflections in both alloys, close to the positions of the 111-type reflections of the B19' martensite (some examples are marked by arrows in Fig. 5c). In all cases, the main reflections observed in the SADPs correspond to the cubic B2 phase, proving that this is the average crystal struc-

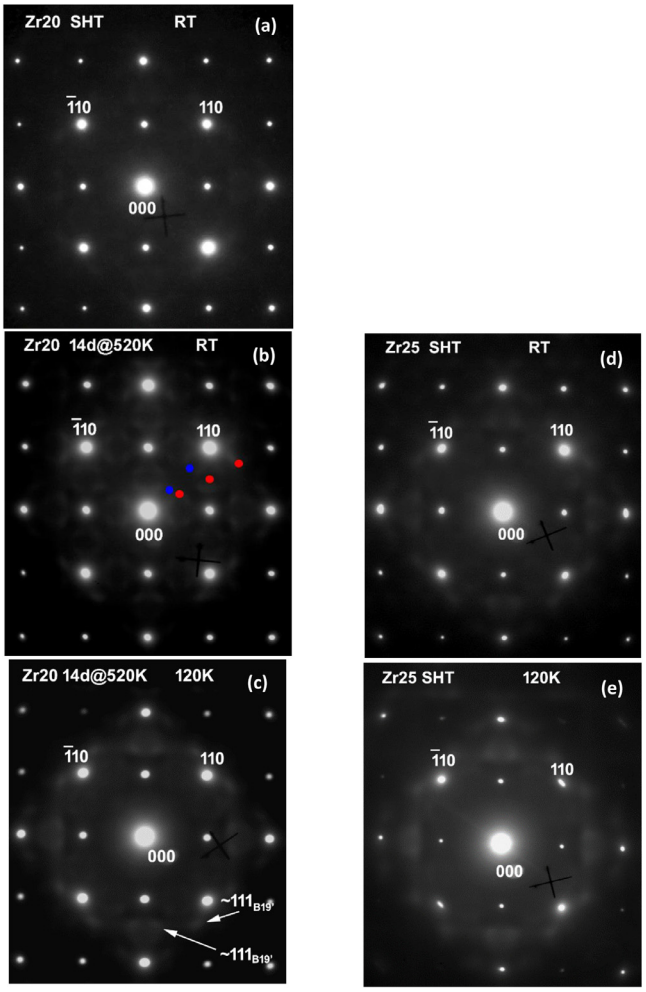

Fig. 5. Selected-area electron diffraction patterns (SADP) along the [001] zone axis of the $Ni_{50.3}Ti_{29.7}Zr_{20}$ alloy in the SHT state at room temperature (a); $Ni_{50.3}Ti_{29.7}Zr_{20}$ aged at 520 K for 14 days obtained at (b) room temperature and (c) at 120 K and of the $Ni_{50.9}Ti_{24.1}Zr_{25}$ alloy in the SHT state obtained at (d) room temperature and (e) at 120 K. The blue and red spots in Fig 5b indicate the positions of the 1/3[110] and 1/4[210]-type satellites characteristic of the H phase.

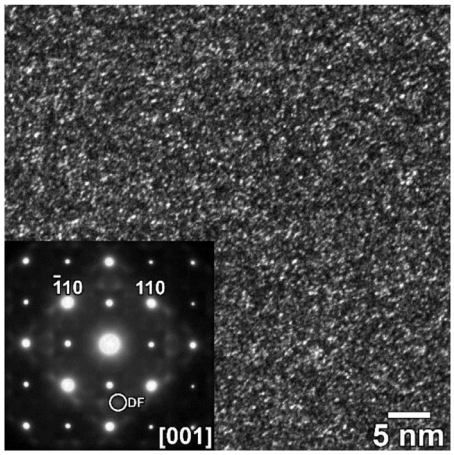

Fig. 6. Dark-field TEM image of $Ni_{50.3}Ti_{29.7}Zr_{20}$ alloy SHT and aged at 520 K for 14 days, taken at 120 K with the diffuse spot marked by a circle in the inserted diffraction pattern.

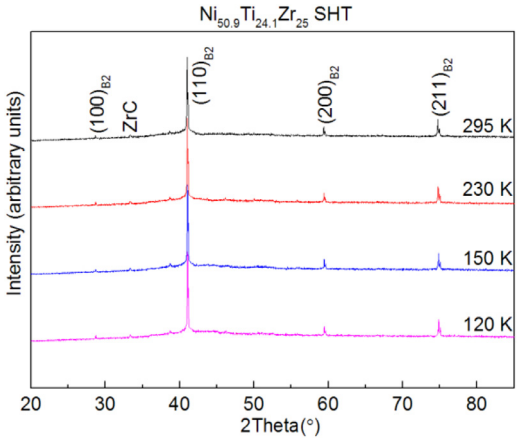

Fig. 7. X-ray diffraction spectra of the $Ni_{50.9}Ti_{24.1}Zr_{25}$ alloy obtained at different temperatures.

ture at low temperatures. In addition, the dark-field TEM images taken at 120 K using one of the diffuse spots clearly reveals the existence of small martensitic-like nanodomains, as shown in Fig. 6. These features are also commonly accepted as evidences of the strain glass state [1,15,23–25].

Fig. 7 presents X-ray diffraction spectra recorded at temperatures between 295 and 120 K. The results confirm that the average structure at low temperature is the B2 austenite. Indeed, all spectra only contain the cubic B2 reflections and tiny peaks consistent with the ZrC phase. The intensity of the 110 peak in relation to the other fundamental reflections of B2 phase (200, 211) is high, which indicates the existence of texture in the material, developed as a result of the extrusion process.

3.3. Compressive stress-strain response

Alloys in the SG state are known to undergo a stress-induced martensitic transformation and exhibit the related shape memory and superelastic effects [18,19,50–55]. Therefore, these effects have been investigated in the $Ni_{50.3}Ti_{29.7}Zr_{20}$ alloy. Fig. 8a is a series of stress-strain (σ–ε) curves in compression for a SHT sample at different temperatures. The curves are typical of a material undergoing a stress-induced martensitic transformation and exhibit the typical hysteresis loop shape with a well-defined transformation "plateau" with low hardening regime after the onset of inelastic deformation. In contrast, the σ–ε curves for the sample aged for 14 days at 520 K, in the SG state, consist of a smooth loop with little or no plateau and narrower hysteresis (Fig. 8b). Interestingly, for the sample aged for 10 days at 520 K (with suppressed transformation in the DSC but not a well-defined SG state in the DMA tests, Fig. 2c), the σ–ε curves present an intermediate case (Fig. 8c). Regardless, in all three cases for the $Ni_{50.3}Ti_{29.7}Zr_{20}$ alloy, applied strain levels above 4% were fully recovered upon unloading.

A similar transition in the superelastic behavior from loops with a distinct plateau region to smooth loops without plateau and smaller hysteresis width in the SG state was reported in the Ni-Fe-Ga system with increasing Co doping [18] and in Ti-Nb-O with excess O content [53]. This has been interpreted in terms of the peculiar microstructure of the unfrozen strain glass, composed of dynamically disordered local strain domains that induce local fluctuation of the stress field in the system. Under the uniaxial stress, the induced martensite variants are oriented along one direction, leading to formation of long-range inhomogeneous strain/stress fields in the residual untransformed material. Thus, an extra external stress must be provided to overcome such inhomogeneous stress fields, leading to the smooth hysteresis loop [18].

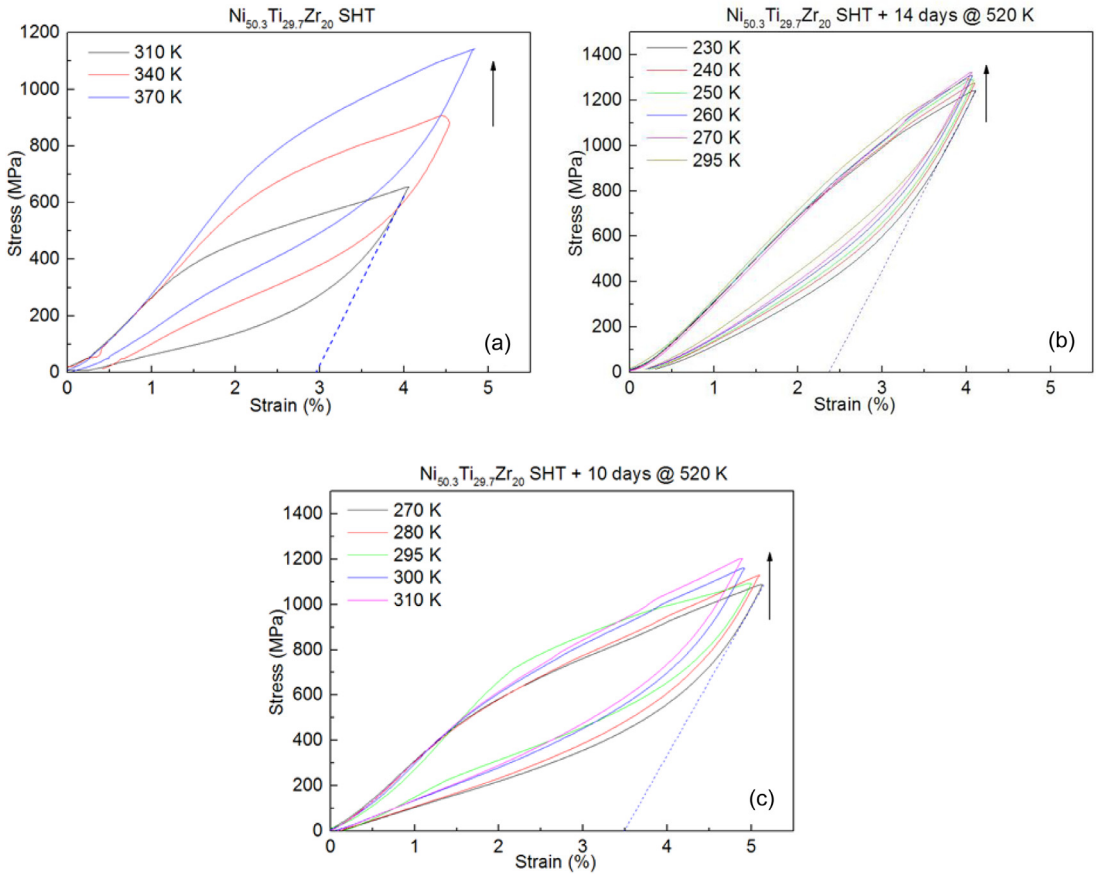

Fig. 8. Compression stress-strain curves at different temperatures for the $Ni_{50.3}Ti_{29.7}Zr_{20}$ alloy in the (a) SHT state and after ageing at 520 K for (b) 14 days and (c) 10 days.

Another interesting observation in Fig. 8b is the very limited temperature dependence exhibited by the smooth hysteresis loops in the sample with well-established strain glass. This is in contrast with the significant shift to increasing stress levels of the transformation plateau with increasing temperature in the sample with normal martensitic transformation (Fig. 8a), which is well explained by the Clausius-Clapeyron equation for first order transitions. The sample with an incomplete SG state (Fig. 8c) shows an intermediate temperature dependence between the two extreme cases.

4. Discussion of the results

The experimental evidences shown above indicate the existence of the strain glass state in the Ni-Ti-Zr system after suitable thermal treatments, which can be linked with the early stages of the H-phase precipitation. This can be rationalized as follows. The crystal structure of the H-phase is, essentially, a superstructure derived from the B2 structure with a redistribution of the Ti and Zr atoms. In the B2 austenite phase, such atoms occupy fully random positions in their sublattice, whereas in the H-phase they develop an ordered supercell with 3-fold, 4-fold and 2-fold periodicities along the $<110>_{B2}$, $<210>_{B2}$ and $<111>_{B2}$ directions, respectively, resulting in the corresponding sharp satellite spots in the diffraction patterns [47,48]. The positions of the 1/3[110] and 1/4[210]-type satellites for one orientation variant of the H phase are indicated in Fig. 5b by blue and red spots, respectively. The H-phase precipitates grow in multiple orientation variants, which produce superlattice spots along all the equivalent directions of the <110>, <210> and <111> families in the diffraction patterns [48]. Moreover, for the composition of alloy 1 ($Ni_{50.3}Ti_{29.7}Zr_{20}$), precipitates with the well-formed H-phase superstructure have been only observed after thermal treatments at 720 K or higher temperatures [35,38,48]. Diffuse streaking in electron diffraction patterns is usually indicative of short-range reordering processes [56]. As shown in Fig. 5b, the diffuse streaks observed after 14 days ageing at 520 K are not coincident with the positions of the H-phase superlattice spots, but rather close to them. This suggests that the limited diffusion at 520 K only permits short range processes that can be considered as the preliminary stages of the Zr and Ti redistribution towards the H phase. Taking into account that the H-phase is richer in Zr, lean in Ti and slightly richer in Ni, compared to the B2 austenite [48], the process at 520 K likely consists of a short range segregation of Zr and Ti atoms leading to the formation of very small domains with modified composition (roughly nanometric in size), but still too small for the complete development of the H phase superstructure with the 3-fold and 4-fold periodicities (note that one lattice parameter of the H phase unit cell is as large as ~2.6 nm [48]). These precursor H-phase would generate a very fine spatial heterogeneity with random strain fields that suppress the normal martensitic transformation and create the strain glass state.

In comparison, alloy 2 ($Ni_{50.9}Ti_{24.1}Zr_{25}$) is richer in Ni and Zr than alloy 1 and lean in Ti, *i.e.* it is closer to the composition of the H-phase [48] and, consequently, has a greater driving force for H-phase precipitation. Therefore, the observation of a suppressed martensitic transition and the strain glass state in this alloy just after the solution heat treatment and quenching, with no need of additional ageing, further supports the link between the origin of the strain glass state and the initial stages of H-phase precipitation. In this case, the precursor nuclei of H-phase are formed during the quenching process after the solution heat treatment. It is

worth noting that the SG state in both Ni-rich Ni-Ti-Zr alloys only exists with this precursor H-phase. If well-developed H-phase precipitates with sizes around 5–10 nm or above (resulting in sharp satellites in the diffraction patterns) are formed by suitable thermal treatments, then a normal martensitic transformation takes place instead of formation of strain glass state [35,38].

The present results constitute another example of strain glass state induced by the onset of a nanoprecipitation process, similar to the observations in Ni-rich Ni-Ti binary alloys with Ni_4Ti_3-type precipitation [7,55,57,58]. As in the present Ni-Ti-Zr alloys, the suppressed martensitic transformation and SG state in the binary alloys is only reported for the initial stages of Ni_4Ti_3 precipitation with finely dispersed nanometric particles, whereas the normal ferroelastic transition is recovered in the presence of larger precipitates [59]. Nevertheless, there is a remarkable difference between both systems. In the binary alloys, the Ni_4Ti_3 precipitates promote the transformation to the R phase, because this phase accommodates the strain field around the precipitates better than the B19' structure [60]. By careful control of alloy composition and thermal treatment, Zhou et al. showed that the SG state induced by nanoprecipitation is at the boundary between the B2-B19' and B2-R phase transitions [57]. In the frozen SG state of the binary alloys, the diffuse spots formed in the diffraction patterns indicate the development of R phase-like nanodomains [7,58]. In contrast, the ternary Ni-rich Ni-Ti-Zr alloys transform to the B19' martensite irrespective of the presence or not of the H-phase and its particle size [38,41]. Fine H-phase nanoprecipitates are fully coherent with the austenite B2 matrix and there is a small lattice misfit between the two phases [48]. As a result, the strain fields around the precipitates are relatively low and can be accommodated in the B19' martensite phase [48], with no need to develop an "intermediate" phase analogous to the R-phase of the binary alloys. Consequently, the nanodomains and diffuse diffraction spots observed in the frozen strain glass state of the present Ni-Ti-Zr alloys are B19'-like instead of R-like (Fig. 5c,d). Existence of B19'-type SG was also reported in binary $Ni_{50.8}Ti_{49.2}$ alloys after cold rolling with thickness reduction levels of 27% or above and it was attributed to the dislocation arrays formed after cold rolling, which constitute extended defects that impose effective nanoconfinement of the B19' domains [9]. Similar to the present Ni-Ti-Zr alloys, quasilinear σ–ε curves with no plateau, high strength (1.2 GPa) and recoverable strains around 4% were obtained in the B19'-type SG induced by cold rolling [9].

The shapes of the σ–ε curves of strain glasses reported in literature show wide variability. For some cases corresponding to SG induced in binary NiTi alloys by high Ni doping [50,51] or Ni_4Ti_3 nanoprecipitates [55], curves with a sharp plateau and large recoverable strains above 6% are reported, which are attributed to the reversible stress-induced transition to B19' martensite. In these cases, the yield stress exhibits temperature dependence. In constrast, for the SG induced by cold rolling in $Ni_{50.8}Ti_{49.2}$ [9] or by the precursor H phase in the present Ni-Ti-Zr alloys, both composed of B19'-type nanodomains, smooth σ–ε loops with no plateau and very little dependence on temperature are obtained. The quasilinear deformation suggests the existence of a broad spectrum of defects responsible for the SG (either dislocations networks with different size/density or precursor H-phase nanodomains with different size, local composition, inter-domain distance and strain fields in the surrounding B2 matrix) that create a broad distribution of local M_s values for the martensitic transformation (and σ_s values for the stress-induced transition) in the B2 matrix at a fine scale. As a result, an increasing number of B19'-like nanodomains would be formed upon cooling. The microstructure of the present Ni-Ti-Zr alloys in the SG state is schematized in Fig. 9 for four levels of increasing stress, $0 < \sigma_1 < \sigma_2 < \sigma_3$. The black ellipses represent the precursor H-phase nanodomains responsible for the SG state, while the B19'-like nanodomains are represented by ellipses of different colors, corresponding to different orientation variants. Application of stress causes two effects: (*i*) growth of the nanodomains of the variant favored by the direction of the applied stress, represented in blue color in Fig. 9, which implies the stress-induced transformation of the surrounding B2 matrix, and (*ii*) reorientation of the other nanodomains towards the favored variant. The precursor H-phase and martensitic nanodomains of other variants limit the stress-induced growth of blue domains to the low spatial scale, even under the highest stress levels (as schematized in Fig. 9), which reduces the macroscopic strain to $\sim$ 4% in the present case, below the maximum strain levels achieved in the normal B2-B19' transition ($\sim$6−10%).

To understand the structural evolution under stress at different temperatures, we may consider the typical temperature dependence of the apparent yield stress (onset of inelastic deformation) shown by alloys with martensitic transformation, schematized in Fig. 10a. Above the M_s temperature, the stress increases linearly with temperature according to the Clausius-Clapeyron equation for the stress-induced transformation (red line in Fig. 10a). Below the transition point, there is usually a lower temperature dependence with negative slope, related to the variant reorientation process in martensite (also referred to as detwinning) [61,62], represented by the blue line. Assuming a broad distribution of local M_s values at a fine spatial scale, the phase diagram takes the form shown in Fig. 10b, where a discrete set of transformation/reorientation lines corresponding to different local M_s values (M_{s1}, M_{s2} ..., M_{s7}) are drawn. The distribution of local M_s values is schematically represented by the green Gaussian-type curve. The transformation/reorientation lines corresponding to local M_s values located at the tails of the distribution curve are drawn in thinner lines, to visualize the fact that they have low "populations" and, then, involve a low volume fraction of material. A mechanical test performed at a certain temperature can be represented by a vertical line. In such a phase diagram, the vertical lines continuously intersect red or blue lines, producing either growth of favored martensitic nanodomains or reorientation of non-favored ones, respectively. These events develop discrete amounts of strain proportional to the population of their local M_s value in the broad distribution. As a result, the macroscopic σ-ε curves are quasilinear in shape with no "plateau". Moreover, for a temperature interval located around the center of the distribution, represented by the vertical lines at temperatures T_1 and T_2 in Fig. 10b, most of red/blue lines intercepted in a wide stress range correspond to local M_s values with similar populations, producing similar amounts of macroscopic deformation. Therefore, macroscopic σ-ε curves with little temperature dependence can be expected from this qualitative model, as observed in the present Ni-Ti-Zr alloys (Fig. 8b). It is worth noting that at high temperatures (around T_2), the reorientation events only play a significant role for low stress levels and the transformation process is dominating at high stresses. However, as temperature decreases and approaches T_1, the contribution of the reorientation process extends to higher stress levels whereas the transformation events at high stresses become less significant, as they involve low local M_s values with lower population.

The DMA results presented in Figs. 2 and 3 show a temperature independence of the storage modulus over wide temperature ranges, suggesting the existence of the *elinvar* effect in the present Ni-Ti-Zr alloys. This effect was first reported one hundred years ago in Fe-Ni-Cr ferromagnetic alloys [63] and later in non-magnetic multifunctional β-Ti alloys [64]. More recently, the *elinvar* effect has been linked with the strain glass state in these Ti-based alloys [65] and also in doped Ni-Ti alloys [66,67]. In Ref. [67], the effect is explained in terms of the competition between the normal behavior of crystalline solids (modulus increase upon cooling related to anharmonic atomic vibrations) and the well-known soft-

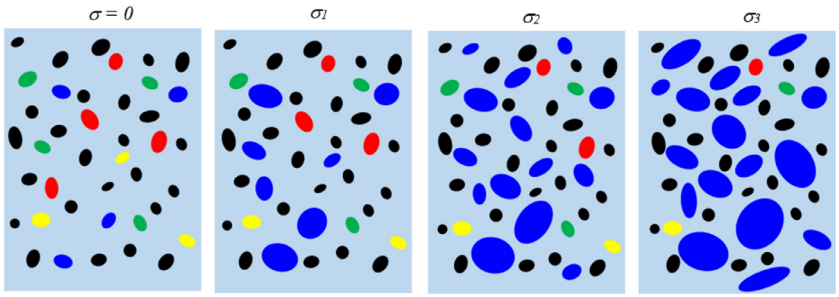

Fig. 9. Schematic representation of the microstructure of the Ni-Ti-Zr alloys at increasing stress levels $0 < \sigma_1 < \sigma_2 < \sigma_3$. Black ellipses represent the precursor H-phase nanodomains, while green, red, yellow and blue features represent B19'-like nanodomains of four different variants.

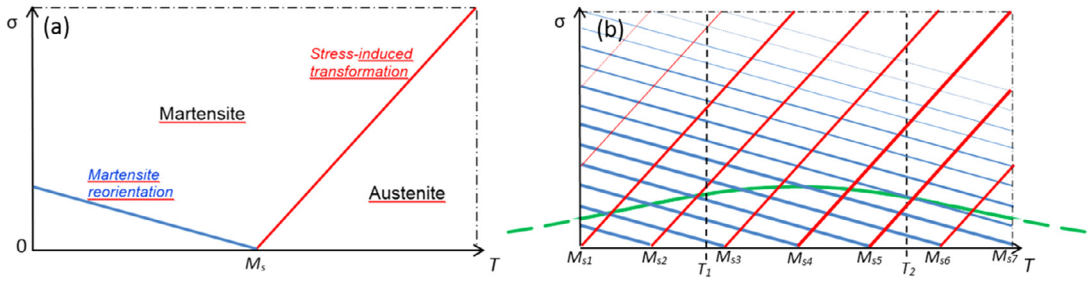

Fig. 10. (a) Schematic plot of the critical stress for martensite reorientation (blue line) and stress-induced transformation (red line) in an alloy with normal martensitic transformation. (b) Schematic phase diagram of an alloy with a broad distribution of local M_s values, where the critical stress lines for a discrete set of values M_{s1}, M_{s2} ..., M_{s7} are drawn. The distribution of local M_s values is represented by the green Gauss-type curve.

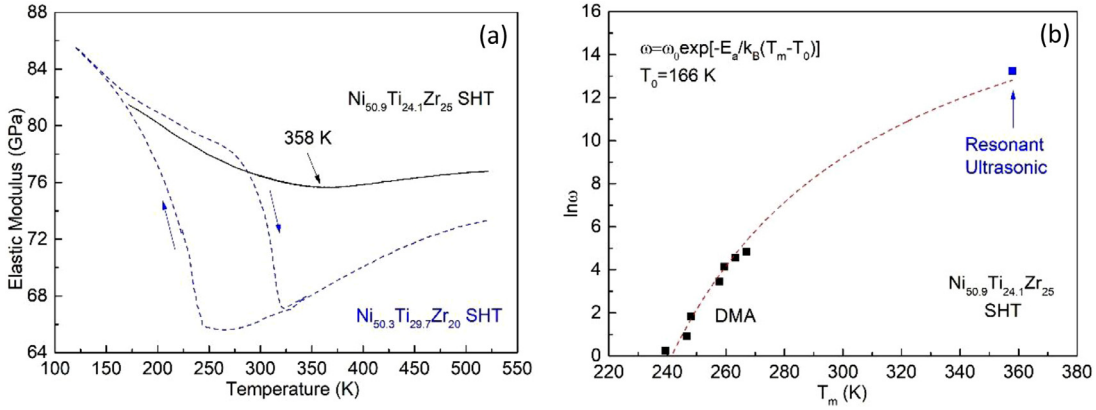

Fig. 11. (a) Elastic modulus measured by the resonant ultrasonic technique [68] for $Ni_{50.9}Ti_{24.1}Zr_{25}$ SHT in the strain glass state (solid line) and for $Ni_{50.3}Ti_{29.7}Zr_{20}$ SHT with normal martensitic transformation (dashed line). (b) Extended semilogarithmic plot of the frequencies as a function of T_m for $Ni_{50.9}Ti_{24.1}Zr_{25}$ SHT.

ening effect of the austenite phase when approaching the martensitic transformation temperature. In the temperature region corresponding to the unfrozen strain glass state there is a gradual and moderate softening effect related to the broad distribution of local M_s values and the gradual formation of martensite-like nanodomains that compensates for the normal modulus hardening and causes the *elinvar* effect over a wide temperature range [67]. This could be a plausible explanation of the effect observed in Figs. 2e,f and 3, corresponding to the unfrozen strain glass of alloys 1 and 2. However, the same effect is also present in the DMA curves of non-aged SHT alloy 1 (Fig. 2a), which undergoes the normal martensitic transformation instead of SG behavior.

In view of this complex behavior and considering that the DMA technique has a limited accuracy for the elastic modulus measurement of rigid metals, additional experiments using a resonant ultrasonic technique were undertaken. The elastic modulus is obtained from the measurement of the resonance frequency of vibration of a composed oscillator formed by a quartz crystal attached to the sample (see Ref. [68] for details), which allows for a much higher accuracy than the DMA technique based on the measurement of stress and strain. However, the technique works under resonance condition, close to 100 kHz, which does not allow the exploration of different frequency ranges in the same sample. Samples of both alloys in the SHT state (alloy 2 with a well-developed SG state and alloy 1 with normal transformation) were tested in a wide temperature interval and the results are shown in Fig. 11a. As expected, alloy 2 with SG (solid line) exhibits a decreasing elastic modulus with increasing temperature reaching a slight minimum before entering a plateau region and alloy 1 (dashed line) shows the traces of the forward and reverse martensitic transformation with hysteresis. It is worth noting that the levels of E modulus measured by the resonant technique, above 65 GPa, are significantly larger than those obtained by DMA in the same materials (Figs. 2, 3), which is primarily due to the low accuracy in the strain measurement in DMA. As clearly shown in Fig. 11a, the $Ni_{50.9}Ti_{24.1}Zr_{25}$ alloy in the SG state presents a very slight temperature dependence of the elastic modulus in the high temperature side above the minimum. Though the curve is not completely

flat, the *E* modulus only presents a small change of 1.16 GPa over a temperature interval of 164 K, giving a rate of 0.007 GPa/K. In turn, the $Ni_{50.3}Ti_{29.7}Zr_{20}$ alloy with normal transformation shows a much larger temperature dependence in the austenite state; the elastic modulus decreases at a rate of 0.030 GPa/K (7.7 GPa in 255 K). Therefore, the more accurate measurements confirm an *elinvar* behavior of the Ni-rich Ni-Ti-Zr alloys only under a well-established strain glass state, and the typical modulus softening in the normal condition. This confirms the mechanism of the *elinvar* effect proposed in Ref. [67], based on compensation between a gradual and moderate softening effect related to the gradual formation of B19'-like nanodomains upon cooling and the normal modulus hardening related to phonon anharmonic effects.

The modulus minumum of the $Ni_{50.9}Ti_{24.1}Zr_{25}$ alloy with SG state is shifted to 358 K as a result of the frequency dependence and the high frequency levels used in this experiment (88,490 Hz). The present temperature for minimum modulus and the results of DMA experiments shown in Fig. 3a are plotted together, based on the Vogel-Fulcher relationship, in Fig. 11b. The reasonable fit to the data demonstrates that the exponential dependence extends up to the high frequency range, completely ruling out a linear relationship, though the ideal T_0 temperature fitted from the combined plot, $T_0 = 166$ K, deviates from the value based on DMA only (220 K, Fig. 3). The discrepancy is probably due to the combination of data obtained from methods with different resolution and the lack of data in the intermediate frequency range.

5. Summary and conclusions

The present work demonstrates the existence of the strain glass (SG) state in $Ni_{50.3}Ti_{29.7}Zr_{20}$ and $Ni_{50.9}Ti_{24.1}Zr_{25}$ polycrystalline alloys. The main findings can be summarized as follows:

1 The strain glass state in Ni-rich Ni-Ti-Zr alloys can be linked to the early stages of H-phase precipitation. For $Ni_{50.3}Ti_{29.7}Zr_{20}$, the normal martensitic transformation occurs after solution heat treatment, whereas the SG state is detected by DMA experiments after additional 14 days ageing at 520 K. The low temperature ageing promotes a short-range segregation of Zr and Ti atoms leading to the formation of precursor nuclei of the H phase. These small nuclei are responsible for the very fine spatial heterogeneity inherent to the strain glass state. The $Ni_{50.9}Ti_{24.1}Zr_{25}$ alloy is closer in composition to the H-phase and, therefore, the driving force for precipitation is greater. Consequently, the short-range atomic segregation already occurs upon quenching from the solution heat treatment temperature and the SG state is observed in this alloy just after this treatment, with no need of additional low-temperature ageing.
2 The strain glass in Ni-rich Ni-Ti-Zr alloys is related to B19'-type nanodomains, similar to the SG induced by cold rolling in binary Ni-Ti [9]. This is in contrast to other Ni-Ti-based alloys for which the nanodomains are of R phase type.
3 The DMA results show a temperature independence of the storage modulus over wide temperature ranges, suggesting the existence of the *elinvar* effect in the studied Ni-Ti-Zr alloys both in the SG and normal states. More accurate measurements using a resonant ultrasonic technique have confirmed an *elinvar* effect in the SG state (very low temperature dependence of the elastic modulus) and the typical modulus softening in the state exhibiting normal martensitic transformation. These observations confirm the mechanism of the *elinvar* effect proposed in Ref. [67]. Moreover, the ultrasonic measurements confirm the exponential frequency dependence in the SG state (Vogel-Fulcher relationship) over a wide frequency interval up to 10^4 Hz.
4 Superelastic behavior has been observed in the strain glass state of the $Ni_{50.3}Ti_{29.7}Zr_{20}$ alloy, consistent with other strain glass systems. The mechanical response of the Ni-Ti-Zr strain glass in compression shows smooth and quasilinear σ-ε curves and recoverable strains of over 4% with very little temperature dependence. This behavior can be of great interest for practical applications in devices designed to perform a constant mechanical response over a broad range of temperatures.
5 The mechanical response can be qualitatively interpreted assuming a large heterogeneity in the defects responsible for the SG state that creates a wide distribution of local martensitic transformation temperatures in the B2 matrix at fine spatial scale, together with the coexistence of deformation mechanisms based on stress-induced transformation and variant reorientation processes with opposite temperature dependences.

Declaration of Competing Interest

The authors declare that they have no known competing financial interests or personal relationships that could have appeared to influence the work reported in this paper.

Acknowledgments

The authors deeply acknowledge Dr. Sergey Kustov for his assistance in the resonant ultrasonic measurements of elastic modulus. The work was supported by Spanish Ministerio de Ciencia, Innovación y Universidades - Agencia Estatal de Investigación (MCIU-AEI) and Fondo Europeo de Desarrollo Regional (FEDER), EU (project RTI 2018-094683-B-C51). Additional support for this work was provided by the NASA Transformative Aeronautics Concepts Program (TACP), Transformational Tools & Technologies Project. IK acknowledges the supports from the US Air Force Office of Scientific Research, under Grant no. FA9550-18-1-0276 and the US National Science Foundation, Grant No. CMMI-1917367.

References

[1] S. Sarkar, X. Ren, K. Otsuka, Evidence for strain glass in the ferroelastic–martensitic system $Ti_{50-x}Ni_{50+x}$, Phys. Rev. Lett. 95 (2005) 205702.
[2] Y. Zhou, D. Xue, X. Ding, Y. Wang, J. Zhang, Z. Zhang, D. Wang, K. Otsuka, J. Sun, X. Ren, Strain glass in doped Ti50 ($Ni_{50-x}D_x$)(D= Co, Cr, Mn) alloys: implication for the generality of strain glass in defect-containing ferroelastic systems, Acta Mater. 58 (2010) 5433–5442.
[3] D. Wang, Z. Zhang, J. Zhang, Y. Zhou, Y. Wang, X. Ding, Y. Wang, X. Ren, Strain glass in Fe-doped Ti–Ni, Acta Mater. 58 (2010) 6206–6215.
[4] B. Ramachandran, P.C. Chang, Y.K. Kuo, C. Chien, S.K. Wu, Characteristics of martensitic and strain-glass transitions of the Fe-substituted TiNi shape memory alloys probed by transport and thermal measurements, Sci. Rep. 7 (2017) 16336.
[5] S. Ren, C. Zhou, D. Xue, D. Wang, J. Zhang, X. Ding, K. Otsuka, X. Ren, Sandwichlike strain glass phase diagram of $Ti_{49}Ni_{51-x}Pdx$, Phys. Rev. B 94 (2016) 214112.
[6] G.Y. Liao, B. Chen, Q.K. Meng, M.J. Wang, X.Q. Zhao, Strain glass in defect-containing ferroelastic $Ti_{44}Ni_{51}Nb_5$ alloy, Rare Met. 34 (2015) 829–832.
[7] Y.C. Ji, X.D. Ding, T. Lookman, K. Otsuka, X.B. Ren, Heterogeneities and strain glass behavior: role of nanoscale precipitates in low-temperature-aged $Ti_{48.7}Ni_{51.3}$ alloys, Phys. Rev. B 87 (2013) 104110.
[8] J. Zhang, D. Xue, X. Cai, X. Ding, X. Ren, J. Sun, Dislocation induced strain glass in $Ti_{50}Ni_{45}Fe_5$ alloy, Acta Mater. 120 (2016) 130–137.
[9] Q. Liang, D. Wang, J. Zhang, Y. Ji, X. Ding, Y. Wang, X. Ren, Y. Wang, Novel B19' strain glass with large recoverable strain, Phys. Rev. Mater. 1 (2017) 033608.
[10] J.A. Monroe, J.E. Raymond, X. Xu, M. Nagasako, R. Kainuma, Y.I. Chumlyakov, R. Arroyave, I. Karaman, Multiple ferroic glasses via ordering, Acta Mater. 101 (2015) 107–115.
[11] H. Ma, J. Yang, F. Lu, F. Qin, W. Xiao, X. Zhao, A FeNiMnC alloy with strain glass transition, Prog. Nat. Sci. Mater. Int. 28 (2018) 74–77.
[12] S. Ren, D. Xue, Y. Ji, X. Liu, S. Yang, X. Ren, Low-field-triggered large magnetostriction in iron-palladium strain glass alloys, Phys. Rev. Lett. 119 (2017) 125701.
[13] Y. Zhou, D. Xue, X. Ding, K. Otsuka, J. Sun, X. Ren, High temperature strain glass in Ti 50 ($Pd_{50-x}Cr_x$) alloy and the associated shape memory effect and superelasticity, Appl. Phys. Lett. 95 (2009) 151906.
[14] Y. Wang, J. Gao, H. Wu, S. Yang, X. Ding, D. Wang, X. Ren, Y. Wang, X. Song, J. Gao, Strain glass transition in a multifunctional β-type Ti alloy, Sci. Rep. 4 (2014) 3995.

[15] Y. Zhou, D. Xue, Y. Tian, X. Ding, S. Guo, K. Otsuka, J. Sun, X. Ren, Direct evidence for local symmetry breaking during a strain glass transition, Phys. Rev. Lett. 112 (2014) 025701.

[16] Y. Wang, C. Huang, J. Gao, S. Yang, X. Ding, X. Song, X. Ren, Evidence for ferromagnetic strain glass in Ni-Co-Mn-Ga heusler alloy system, Appl. Phys. Lett. 101 (2012) 101913.

[17] Y. Wang, C. Huang, H. Wu, J. Gao, S. Yang, D. Wang, X. Ding, X. Song, X. Ren, Spontaneous strain glass to martensite transition in ferromagnetic Ni-Co-Mn-Ga strain glass, Appl. Phys. Lett. 102 (2013) 141909.

[18] D.P. Wang, X. Chen, Z.H. Nie, N. Li, Z.L. Wang, Y. Ren, Y.D. Wang, Transition in superelasticity for $Ni_{55-x}Co_xFe_{18}Ga_{27}$ alloys due to strain glass transition, Europhys. Lett. 98 (2012) 46004.

[19] Q.H. Zhang, Z. Zhai, Z.H. Nie, S. Harjo, D.Y. Cong, M.G. Wang, J. Lie, Y.D. Wang, An *in situ* neutron diffraction study of anomalous superelasticity in a strain glass $Ni_{43}Fe_{18}Ga_{27}Co_{12}$ alloy, J. Appl. Cryst. 48 (2015) 1183–1191.

[20] Z. Wu, Strain glass behavior of Ni–Co–Mn–Sn ferromagnetic shape memory alloys, Phys. Status Solid RRL 9 (2015) 317–320.

[21] P.J. Stonaha, I. Karaman, R. Arroyave, D. Salas, N.M. Bruno, Y. Wang, M.F. Chisholm, S. Chi, D.L. Abernathy, Y.I. Chumlyakov, M.E. Manley, Glassy phonon heralds a strain glass state in a shape memory alloy, Phys. Rev. Lett. 120 (24) (2021) 245701.

[22] S. Kustov, D. Salas, E. Cesari, R. Santamarta, D. Mari, J. Van Humbeeck, Structural anelasticity, elasticity and broken ergodicity in Ni–Ti shape memory alloys, Acta Mater. 73 (2014) 275–286.

[23] J. Zhang, Y. Wang, X. Ding, Z. Zhang, Y. Zhou, X. Ren, D. Wang, Y. Ji, M. Song, K. Otsuka, J. Sun, Spontaneous strain glass to martensite transition in a $Ti_{50}Ni_{44.5}Fe_{5.5}$ strain glass, Phys. Rev. B 84 (2011) 214201.

[24] S. Hou, Y. Wang, J. Zhang, D. Wang, S. Ren, X. Ren, Evidence for crossover martensite in $Ti_{50}Ni_{45}Fe_5$: an intermediate state between normal martensite and strain glass, EPL 100 (2012) 58001.

[25] J. Lu, G.T. Martinez, S. Van Aert, D. Schryvers, Lattice deformations in quasi-dynamic strain glass visualised and quantified by aberration corrected electron microscopy, Phys. Status Solid B (2014) 1–7.

[26] X.L. Meng, W. Cai, F. Chen, L.C. Zhao, Effect of aging on martensitic transformation and microstructure in Ni-rich TiNiHf shape memory alloy, Scr. Mater. 54 (2006) 1599–1604.

[27] A.M. Sandu, K. Tsuchiya, S. Yamamoto, Y. Todaka, M. Umemoto, Influence of isothermal ageing on mechanical behavior in Ni-rich Ti–Zr–Ni shape memory alloy, Scr. Mater. 55 (2006) 1079–1082.

[28] A.M. Sandu, K. Tsuchiya, M. Tabuchi, S. Yamamoto, Y. Todaka, M. Umemoto, Microstructural evolution during isothermal aging in Ni-Rich Ti-Zr-Ni shape memory alloys, Mater. Trans. 48 (2007) 432–438.

[29] X.L. Meng, W. Cai, Y.D. Fu, Q.F. Li, J.X. Zhang, L.C. Zhao, Shape-memory behaviors in an aged Ni-rich TiNiHf high temperature shape-memory alloy, Intermetallics 16 (2008) 698–705.

[30] H.E. Karaca, S.M. Saghaian, B. Basaran, G.S. Bigelow, R.D. Noebe, Y.I. Chumlyakov, Compressive response of nickel-rich NiTiHf high-temperature shape memory single crystals along the [111]orientation, Scr. Mater. 65 (2011) 577–580.

[31] O. Benafan, R.D. Noebe, S.A. Padula, R. Vaidyanathan, Microstructural Response During Isothermal and Isobaric Loading of a Precipitation-Strengthened Ni-29.7Ti-20Hf High-Temperature Shape Memory Alloy, Metall. Mater. Trans. A 43 (2012) 4539–4552.

[32] D.R. Coughlin, P.J. Phillips, G.S. Bigelow, A. Garg, R.D. Noebe, M.J. Mills, Characterization of the microstructure and mechanical properties of a 50.3Ni–29.7Ti–20Hf shape memory alloy, Scr. Mater. 67 (2012) 112–115.

[33] A. Evirgen, F. Basner, I. Karaman, R.D. Noebe, J. Pons, R. Santamarta, Effect of aging on the martensitic transformation characteristics of a Ni-rich NiTiHf high temperature shape memory alloy, Funct. Mater. Lett. 5 (2012) 1250038.

[34] H.E. Karaca, S.M. Saghaian, G. Ded, H. Tobe, B. Basaran, H.J. Maier, R.D. Noebe, Y.I. Chumlyakov, Effects of nanoprecipitation on the shape memory and material properties of an Ni-rich NiTiHf high temperature shape memory alloy, Acta Mater. 61 (2013) 7422–7431.

[35] A. Evirgen, I. Karaman, R.D. Noebe, R. Santamarta, J. Pons, Effect of precipitation on the microstructure and the shape memory response of the $Ni_{50.3}Ti_{29.7}Zr_{20}$ high temperature shape memory alloy, Scr. Mater. 69 (2013) 354–357.

[36] O. Benafan, A. Garg, R.D. Noebe, G.S. Bigelow, S.A. Padula, D.J. Gaydosh, N. Schell, J.H. Mabe, R. Vaidyanathan, Mechanical and functional behavior of a Ni-rich $Ni_{50.3}Ti_{29.7}Hf_{20}$ high temperature shape memory alloy, Intermetallics 50 (2014) 94–107.

[37] A.P. Stebner, G.S. Bigelow, J. Yang, D.P. Shukla, S.M. Saghaian, R. Rogers, A. Garg, H.E. Karaca, Y. Chumlyakov, K. Bhattacharya, R.D. Noebe, Transformation strains and temperatures of a nickel–titanium–hafnium high temperature shape memory alloy, Acta Mater. 76 (2014) 40–53.

[38] A. Evirgen, I. Karaman, R. Santamarta, J. Pons, R.D. Noebe, Microstructural characterization and superelastic response of a $Ni_{50.3}Ti_{29.7}Zr_{20}$ high temperature shape memory alloy, Scr. Mater. 81 (2014) 12–15.

[39] K.C. Atli, I. Karaman, R.D. Noebe, G. Bigelow, D. Gaydosh, Work production using the two-way shape memory effect in NiTi and a Ni-rich NiTiHf high-temperature shape memory alloy, Smart Mater. Struct. 24 (2015) 125023.

[40] A. Evirgen, I. Karaman, R. Santamarta, J. Pons, R.D. Noebe, Microstructural characterization and shape memory characteristics of the $Ni_{50.3}Ti_{34.7}Hf_{15}$ shape memory alloy, Acta Mater. 83 (2015) 48–60.

[41] A. Evirgen, I. Karaman, R. Santamarta, J. Pons, C. Hayrettin, R.D. Noebe, Relationship between crystallographic compatibility and thermal hysteresis in Ni-rich NiTiHf and NiTiZr high temperature shape memory alloys, Acta Mater. 121 (2016) 374–383.

[42] L. Patriarca, H. Sehitoglu, E. Yu. Panchenko, Y.I. Chumlyakov, High-temperature functional behavior of single crystal $Ni_{51.2}Ti_{23.4}Hf_{25.4}$ shape memory alloy, Acta Mater. 106 (2016) 333–343.

[43] O. Karakoc, C. Hayrettin, M. Bass, S.J. Wang, D. Canadinc, J.H. Mabe, D.C. Lagoudas, I. Karaman, Effects of upper cycle temperature on the actuation fatigue response of NiTiHf high temperature shape memory alloys, Acta Mater. 138 (2017) 185–197.

[44] N. Babacan, M. Bilal, C. Hayrettin, J. Liu, O. Benafan, I. Karaman, Effects of cold and warm rolling on the shape memory response of $Ni_{50}Ti_{30}Hf_{20}$ high-temperature shape memory alloy, Acta Mater. 157 (2018) 228–244.

[45] O. Karakoc, C. Hayrettin, D. Canadinc, I. Karaman, Role of applied stress level on the actuation fatigue behavior of NiTiHf high temperature shape memory alloys, Acta Mater. 153 (2018) 156–168.

[46] C. Hayrettin, O. Karakoc, I. Karaman, J.H. Mabe, R. Santamarta, J. Pons, Two way shape memory effect in NiTiHf high temperature shape memory alloy tubes, Acta Mater. 163 (2019) 1–13.

[47] F. Yang, D.R. Coughlin, P.J. Phillips, L. Yang, A. Devaraj, R.D. Noebe, M.J. Mills, Structure analysis of a precipitate phase in an Ni-rich high-temperature NiTiHf shape memory alloy, Acta Mater. 61 (2013) 3335–3346.

[48] R. Santamarta, R. Arróyave, J. Pons, A. Evirgen, I. Karaman, H.E. Karaca, R.D. Noebe, TEM study of structural and microstructural characteristics of a precipitate phase in Ni-rich Ni-Ti-Hf and Ni-Ti-Zr shape memory alloys, Acta Mater. 61 (2013) 6191–6206.

[49] A.M. Perez-Sierra, J. Pons, R. Santamarta, I. Karaman, R.D. Noebe, Stability of a Ni-rich Ni-Ti-Zr high temperature shape memory alloy upon low temperature aging and thermal cycling, Scr. Mater. 124 (2016) 47–50.

[50] Y. Wang, X. Ren, K. Otsuka, Shape memory effect and superelasticity in a strain glass alloy, Phys. Rev. Lett. 97 (2006) 225703.

[51] Y. Wang, X. Ren, K. Otsuka, A. Saxena, Temperature–stress phase diagram of strain glass $Ti_{48.5}Ni_{51.5}$, Acta Mater. 56 (2008) 2885–2896.

[52] Y. Zhou, D. Xue, X. Ding, K. Otsuka, J. Sun, X. Ren, High temperature strain glass in $Ti_{50}(Pd_{50-x}Cr_x)$ alloy and the associated shape memory effect and superelasticity, Appl. Phys. Lett. 95 (2009) 151906.

[53] Y. Nii, T. Arima, H.Y. Kim, S. Miyazaki, Effect of randomness on ferroelastic transitions: disorder-induced hysteresis loop rounding in Ti-Nb-O martensitic alloy, Phys. Rev. B 82 (2010) 214104.

[54] J. Zhang, Y. Wang, X. Ding, Z. Zhang, Y. Zhou, X. Ren, K. Otsuka, J. Sun, M. Song, Stress-induced strain glass to martensite (R) transition in a $Ti_{50}Ni_{44.5}Fe_{5.5}$ alloy, Phys. Rev. B 83 (2011) 174204.

[55] Z. Tang, Y. Wanga, X. Liao, D. Wanga, S. Yang, X. Song, Stress dependent transforming behaviors and associated functional properties of a nano-precipitates induced strain glass alloy, J. Alloys Compd. 622 (2015) 622–627.

[56] D.B. Williams, C.B. Carter, Transmission Electron Microscopy: a Textbook for Materials Science, Plenum Press, 1996.

[57] Z. Zhou, J. Cui, X. Ren, Strain glass state as the boundary of two phase transitions, Sci. Rep. 5 (2015) 13377.

[58] C. Chien, C.S. Tsao, S.K. Wu, C.Y. Chang, P.C. Chang, Y.K. Kuo, Characteristics of the strain glass transition in as-quenched and 250°C early-aged $Ti_{48.7}Ni_{51.3}$ shape memory alloy, Acta Mater. 120 (2016) 159–167.

[59] E.Y. Panchenko, Y.I. Chumlyakov, I.V. Kireeva, A.V. Ovsyanniko, H. Sehitoglu, I. Karaman, Y.H.J. Maier, Effect of disperse Ti_3Ni_4 particles on the martensitic transformations in titanium nickelide single crystals, Phys. Met. Metallogr. 106 (2008) 577–589.

[60] N. Zhou, C. Shen, M.F.X. Wagner, G. Eggeler, M.J. Mills, Y. Wang, Effect of Ni_4Ti_3 precipitation on martensitic transformation in Ti–Ni, Acta Mater. 58 (2010) 6685–6694.

[61] J. Ma, I. Karaman, R.D. Noebe, High temperature shape memory alloys, Int. Mater. Rev. 55 (2010) 257–315.

[62] E. Panchenko, A. Tokhmetova, N. Surikov, A. Eftifeeva, A. Tagiltsev, E. Timofeeva, Y. Chumlyakov, G. Gerstein, H.J. Maier, Temperature dependence of martensite variant reorientation in stress-induced martensite aged $Ni_{49}Fe_{18}Ga_{27}Co_6$ single crystals, Scr. Mater. 194 (2021) 113618.

[63] C.E. Guillaume, The anomaly of the nickel-steels, Proc. Phys. Soc. Lond. 32 (1919) 374–404.

[64] T. Saito, T. Furuta, J.H. Hwang, S. Kuramoto, K. Nishino, N. Suzuki, R. Chen, A. Yamada, K. Ito, Y. Seno, T. Nonaka, H. Ikehata, N. Nagasako, C. Iwamoto, Y. Ikuhara, T. Sakuma, Multifunctional alloys obtained via a dislocation-free plastic deformation mechanism, Science 300 (2003) 464–467.

[65] X. Ren, Strain glass and ferroic glass–unusual properties from glassy nano-domains, Phys. Status Solid B 251 (2014) 1982–1992.

[66] C. Jian, X. Ren, Elinvar effect in Co-doped TiNi strain glass alloys, Appl. Phys. Lett. 105 (2014) 061904.

[67] L. Zhang, D. Wang, X. Ren, Y. Wang, A new mechanism for low and temperature-independent elastic modulus, Sci. Rep. 5 (2015) 11477.

[68] S. Kustov, S. Golyandin, A. Ichino, G. Gremaud, A new design of automated piezoelectric composite oscillator technique, Mater. Sci. Eng. A 442 (2006) 532–537.